IMPACT OF DOPING ON THE OPTICAL AND STRUCTURAL PROPERTIES OF SEMICONDUCTOR NANOPARTICLES

Subhi sharma

Guest Faculty, Department of physics ,Naveen Government College

Jarhagon District Mungeli (CG)

N k puraley

Assistant Professor, HOD Department of Physics

Dr Jwala Prasad Mishra

government science college mungeli (CG)

Abstract

Doping is an essential component in the process of modifying the optical and structural characteristics of semiconductor nanoparticles. It has a substantial impact on the electronic band structure, defect states, and overall performance of these nanoparticles when it comes to utilisation in optoelectronic applications. The structural changes, crystallinity, and optical characteristics of semiconductor nanoparticles are investigated in this work and the impacts of different dopants on those qualities are investigated. Changes in lattice properties, crystallite size, and shape are revealed by structural analysis using X-ray diffraction (XRD) and transmission electron microscopy (TEM). These changes are caused by doping-induced strain and defect development. As a result of optical characterisation utilising UV-Vis spectroscopy and photoluminescence (PL) research, shifts in bandgap energy, increase or quenching of emission intensity, and variations in defect-related luminescence have been observed. The findings indicate that controlled doping has the potential to increase charge carrier dynamics, boost photonic characteristics, and optimise the functioning of semiconductor nanoparticles for use in applications such as photovoltaics, light-emitting devices, and sensors.

Keywords: *Doping, Optical, Semiconductor, Nanoparticles*

Introduction

Because of their one-of-a-kind size-dependent optical and electrical capabilities, semiconductor nanoparticles (NPs) have attracted a lot of interest. This is because their qualities make them indispensable in a wide range of technological applications, including photovoltaics, light-emitting devices, and biosensors. Among the many methods that may be used to change and improve these features, doping, which involves introducing foreign atoms into the matrix of the nanoparticle, has emerged as a strong method that can be used to adjust the structural and optical characteristics of the nanoparticles. Doping has an effect on the band structure, defect states, and carrier dynamics of semiconductor nanoparticles, which in turn causes variations in the absorption, emission, and electrical characteristics of these particles. Inducing bandgap

narrowing or widening, increasing photoluminescence efficiency, and modifying carrier recombination dynamics are all possible outcomes of doping, depending on the type of dopant that is used and the concentration of the dopant. The introduction of strain, modification of lattice parameters, and influence on crystallinity are all structural effects that may be caused by doping, which in turn can have an effect on the stability and usefulness of the nanoparticles. The purpose of this research is to evaluate the effect that doping has on the optical and structural properties of semiconductor nanoparticles. More specifically, the investigation will concentrate on the ways in which various dopants modify the crystallographic features, morphology, and light interaction processes of the nanoparticles. These alterations allow us to optimise semiconductor nanoparticles for advanced optoelectronic applications and produce novel materials with specific functions. This is made possible by our knowledge of these modifications.

Structural Modifications Due to Doping

Methods such as X-ray diffraction (XRD), transmission electron microscopy (TEM), and Raman spectroscopy are the primary methods that are utilised in order to investigate the structural alterations that are brought about by doping in semiconductor nanoparticles. As a result of the ionic radius variations that exist between the dopant and host atoms, studies have demonstrated that the inclusion of dopants can not only change the lattice parameters but also create strain and have an effect on the size of the crystallites. In the case of Mn-doped ZnO nanoparticles, for instance, the presence of dopant-induced defects results in an increase in lattice strain and a decrease in crystallinity. Similarly, it has been discovered that the introduction of rare-earth doping into CdS nanoparticles can result in structural distortions that have an impact on the stability and electrical characteristics of the particles.

Optical Property Modifications Due to Doping

Doping has a considerable impact on the optical characteristics of semiconductor nanoparticles, including the absorption and emission spectra of these particles. Research conducted using photoluminescence (PL) and ultraviolet-visible (UV-Vis) spectroscopy reveals that doping can result in either a redshift or a blueshift in the energy of the bandgap, depending on the kind of dopant and the concentration of the agent. For example, the incorporation of transition metals into zinc oxide (ZnO) leads to the narrowing of the bandgap on account of the development of new energy levels within the band structure, which in turn increases the amount of visible light that is absorbed. With rare-earth doping, on the other hand, photoluminescence is frequently increased by the introduction of radiative recombination centres, which ultimately results in enhanced emission intensity and tunability.

Defect Engineering and Charge Carrier Dynamics

Doping also has an effect on the dynamics of charge carriers because it introduces defect states that have an effect on the rates at which carriers recombine. Quantum efficiency can be improved by the use of controlled doping, which can lower the amount of non-radiative recombination. Furthermore, dopant-induced defects have the ability to function as electron traps, which can change the characteristics of charge transport and improve the usefulness of photocatalytic and sensing applications. Recent research on Ag-doped TiO2

nanoparticles has shed light on the role that dopants play in enhancing charge separation and reducing electron-hole recombination, which ultimately results in improved photocatalytic performance.

Experimental Procedures

Materials

Cadmium Chloride ($CdCl_2$) 99.5 %, Sodium Sulphide Nonohydrate ($Na2S.9H2O$) 99%, Merceptoethenol (ME); (C_2H_5OSH) as well as Manganese Chloride (MnCl2) at a concentration of 99% was secured from Aldrich. Every chemical and solvent was utilised in its original state, without any further purification being performed. Wet chemical route approach was used to generate undoped and Mn-doped CdS nanocrystals without any doping. In order to cap the nanoparticles that were synthesised, mercaptoethanol was utilised as a capping agent.

Preparation of CdS Nanoparticles

A round-bottomed flask that was equipped with a reflex cooling tube was used to collect the beginning components in their respective solvents. After that, aqueous solutions of merceptoethenol 0.001 M, Na2S.9H2O 0.01, and CdCl2 have been made. The concentration of each solution is 0.01 M. In the beginning, the aqueous solution of merceptoethenol was injected drop by drop into the solution of CdCl2 at a rate of one millilitre per minute. To stir and reflux the solution under an atmosphere of argon at a temperature of 100 degrees Celsius for two hours, a magnetic stirrer equipped with a hot plate was utilised. Subsequently, a solution of Na2S.9H2O with a concentration of 0.01 M was incrementally added into the solution. The bottom of the flask eventually became occupied by a yellow precipitate that had settled down. The following equation can be used to determine the reaction that has taken place:

$$CdCl_2 + Na_2S9H_2O \longrightarrow CdS + 2NaCl + 9H_2O$$

Due to the fact that the precipitate of CdS is insoluble in water, it was washed many times in double-distilled water prior to being fully cleaned. The presence of mercaptoethanol inhibits the growth of the particles, so preventing them from becoming larger. Centrifugation at a speed of 4000 revolutions per minute for thirty minutes was used to extract the nanoparticles from the reaction media. In the end, the product that was obtained is dried in a vacuum oven at a temperature of 70 degrees Celsius for one hour.

Preparation of Mn Doped CdS Nanoparticle

Distillation, deoxygenation, and deionisation were all performed on the water that was utilised in the preparation. A bubbling process with argon gas was used to accomplish the deoxygenation. On the reaction flask, an aqueous solution of MnCl2 was injected directly into the solution of CdCl2, and then the mixture was refluxed under an atmosphere of Ar at a temperature of 100 degrees Celsius for two hours. Subsequently, a solution of Na2S.9H2O with a concentration of 0.01 M was incrementally added into the solution. The following equation can be used to determine the reaction that has taken place:

$$(1-x)CdCl_2 + xMnCl_2 + Na_2S9H_2O \longrightarrow Cd_{1-x}Mn_xS + 2NaCl + 9H_2O.$$

In order to obtain Mn-doped CdS nanoparticles (3, 4, 6, 8, and 10 weight percent), the weight percentage of Mn was set by adjusting the value of x. The preparation of the samples involved adjusting the amount of

the manganese precursor while maintaining the same amount of sodium sulphide. Following the precipitation of the product samples, the solution was rinsed many times with distilled water and then dried in a vacuum oven at a temperature of 70 degrees Celsius for one hour. In the end, the powder that had been dried was ground. When doing the experiment, it is essential to make use of argon gas and a glove bag in order to prevent the oxidation of manganese. These samples were classified as S1, S2, S3, S4, S5, and S6 respectively. They were synthesised as CdS and Mn doped CdS NPs with weight percentages of 2, 4, 6, 8, and 10 respectively.

Results and discussion

Energy Dispersive X-ray Spectroscopy (EDX) Analysis

Figure 1 depicts the typical EDX spectra of undoped and Mn-doped CdS nanoparticles with weight percentages of 2, 4, 6, 8, and 10 percent. The quantitative weight percentages of the components Cd, S, and Mn that make up the composition of the samples that have been created are displayed according to Table 1.
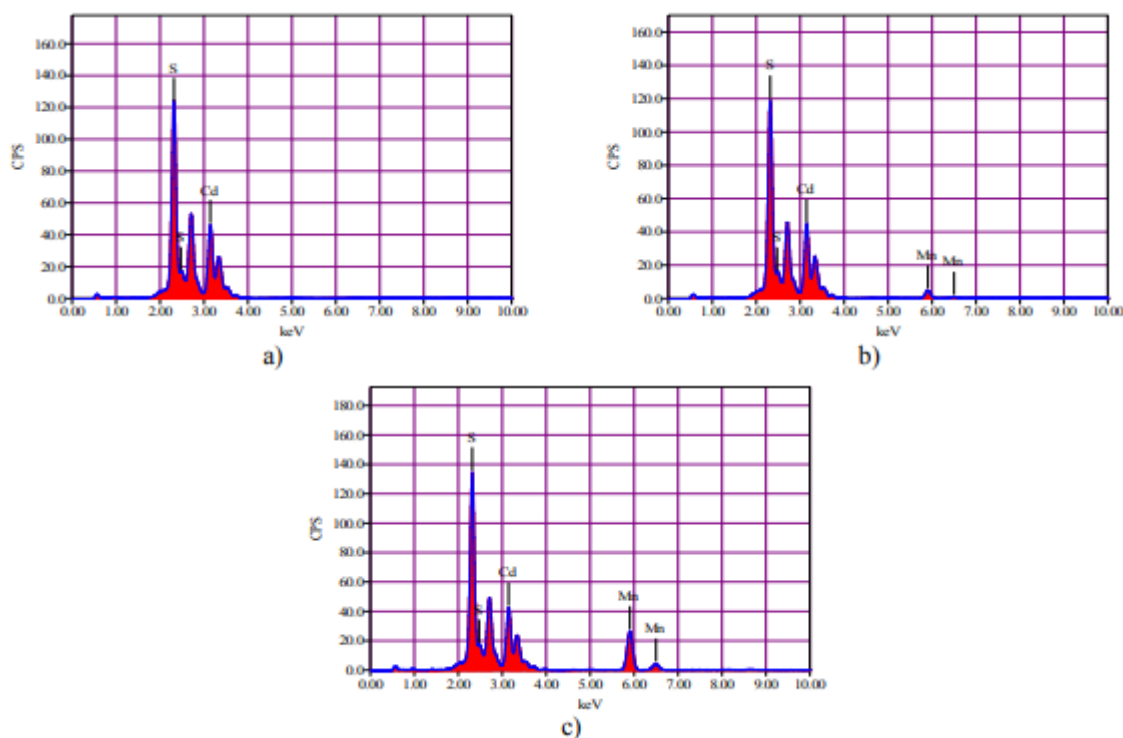
Fig. 1. The energy dispersive x-ray spectra (EDX) of a) CdS, b) CdS:Mn at a weight percentage of two, and c) CdS:Mn at a fraction of ten.

Table 1. EDX compositional analysis of the prepared samples

S. Code	As prepared samples	Elements from EDX analysis in wt%

		Mn	Cd	S
S1	CdS	0	79.06	20.94
S2	CdS: Mn(2wt %)	1.87	75.55	22.58
S3	CdS: Mn(4wt %)	3.69	74.2	22.11
S4	CdS: Mn(6wt %)	5.49	72.6	21.91
S5	CdS: Mn(8wt %)	7.38	70.43	22.19
S6	CdS: Mn(10wt %)	9.46	68.71	21.83

The chemical purity of the samples may be determined by analysing the EDX spectra of undoped and Mn-doped CdS nanoparticles. It is possible to acquire the strong peaks in the spectrum that are associated with Cd, S, and Mn. This demonstrates very clearly that the incorporation of Mn concentrations results in an increase in the strength of the Mn peaks. Variations in compositional homogeneity were found to be the cause of the departure of the estimated elements from the target elements, which was found to be within acceptable limits. Because of this, the EDX spectra exhibit a high degree of concordance with the experimental Mn concentration that was used in the synthesis of NPs.

Structural and Morphology Characterization

There is a diffraction pattern of undoped and Mn-doped CdS nanoparticles displayed in Figure 2. We recorded X-ray diffraction (XRD) spectra at room temperature using a Philips PW 1710 diffractometer. The X-ray diffraction (XRD) spectra were obtained with Cu-Kα radiation at a wavelength of 1.5406 A° and a diffraction angle of 2θ ranging from 10° to 90°. When examining all of the samples that were created, it was seen that there were three diffraction peaks at 2θ values that were close to 26.45 degrees, 43.88 degrees, and 51.97 degrees. These peaks correspond to the reflection from and planes of the cubic phase of the CdS, which is the phase of the material. The produced NPs have an XRD pattern that is identical to the standard cubic CdS (ICCD card No. 04-006-3897). This has been confirmed by XRD analysis. There have been no other phases known to be associated with impurities found. It may be deduced from the fact that all of the diffraction peaks have become more broadened that the products are near the nanoscale. Table 2 contains the results of the computations performed on the samples.
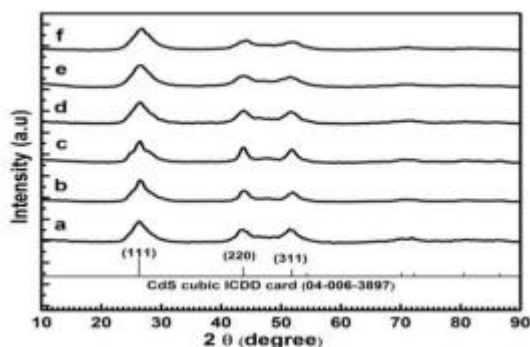
Fig. 2. XRD pattern of a) CdS (b) CdS:Mn (2 wt %), (c) CdS:Mn (4 wt %), (d) CdS:Mn (6 wt %), (e) CdS:Mn (8 wt %) and (f) CdS:Mn (10 wt %).

Table 2 XRD results for synthesized NPs.

Sam p. code	Samp. type	2Θ°	FWHM	(hkl)	d_{111} spacing	Av. Particle size(nm)	Lattice Parameter (a)(nm)	Cell volume $(nm)^3$
S1	CdS	26.34	2.90	(111)	0.3386	7.2	0.586	0.2012
S2	CdS: Mn(2wt %)	26.43	2.96	(111)	0.3369	6	0.583	0.1981
S3	CdS: Mn(4wt %)	26.51	2.98	(111)	0.3359	5.5	0.581	0.1961
S4	CdS: Mn(6wt %)	26.60	3.12	(111)	0.3348	4	0.579	0.1941
S5	CdS: Mn(8wt %)	26.68	3.31	(111)	0.3338	4.4	0.578	0.1931
S6	CdS: Mn(10wt%)	26.68	3.40	(111)	0.3338	4	0.578	0.1931

The Sherrer equation was utilised in order to determine the crystallite size of the samples based on the distribution of the three diffraction peaks;

$$D = \frac{0.9\lambda}{\beta cos\theta} \qquad (1)$$

θ is the Bragg diffraction angle, λ is the x-ray wavelength, and β is the full width at half maximum (FWHM) of the peak. Undoped CdS NPs had a particle size of while Mn-doped NPs (2, 4, 6, 8, and 10 wt %) had a particle size of nm. The addition of Mn to the host CdS lattice does not alter the phase, according to XRD patterns. A change in the location of the host peak, rather than the generation of a new peak adjacent to the host peak, is what Vegard's law predicts. Furthermore, when the Mn concentration increases, the 2 θ position maxima at 26.34, 26.43, 26.51, 26.60, 26.68, and 26.68 degrees indicate a minor increase in shifts to greater angles. It is confirmed that Mn+2 has been incorporated into the CdS lattice by the slight changes

in peak positions. Using the following two equations, the cubic zinc blende lattice parameter (a) is determined for the prepared NPs by applying Bragg's law: ($2dhklSin\theta = n\lambda$), where ($\theta$) is the peak position, (λ) is the wavelength of X-rays, (n) is the order of diffraction (typically n = 1), and (dhkl) is the interplaner separation according to Miller indices hkl:

$$\frac{1}{d_{hkl}^2} = \frac{h^2+k^2+l^2}{a^2} \tag{2}$$

$$a = \frac{\lambda}{2\sin\theta}\sqrt{h^2 + k^2 + l^2} \tag{3}$$

Table 2 shows that when the Mn concentration increases, the unit cell lattice volume decreases significantly. One possible explanation is that the cubic host semiconducting CdS lattice structure has smaller Mn^{+2} ions (0.92 A) instead of bigger Cd^{+2} ions (0.97 A). Figure 3 shows the fluctuation in lattice volumes of the samples doped with Mn.
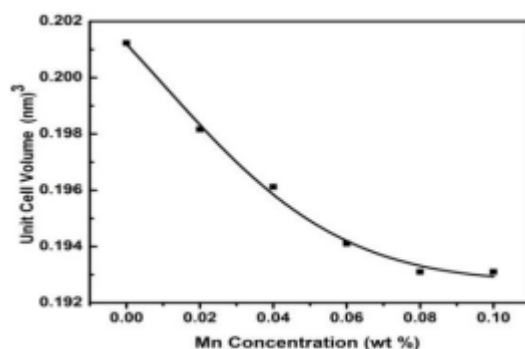
Fig. 3 Difference between undoped and Mn-doped CdS NPs in terms of unit cell volume (nm3)

An HRTEM JEM-2100 (JOEL) system running at an accelerated voltage of 200 KV was used to capture the micrographs of the nanocrystals. The HRTEM pictures were obtained by ultrasonically dispersing the prepared sample in 100% chloroform and then dropping the colloid onto Cu-grid covered with amorphous carbon film. Figure 4 shows HRTEM pictures and size distribution graphs of CdS and CdS:Mn NPs (4, 8, and 10 wt %); from this, we can understand that all of the particles are approximately spherical and have varied sizes. The average particle size of the pure CdS sample was 7.99 nm, whereas that of the samples doped with Mn (4, 8, and 10 wt %) was 6.42 nm, 5.6 nm, and 4.5 nm, respectively. Using a histogram graphic spanning several regions of the HRTEM grid, we were able to approximate the average crystallite size. Particle sizes determined by the Scherrer technique and those determined by the HRTEM analysis were quite congruent. The synthesised NPs' nanodimensional state is further validated by HRTEM investigation.
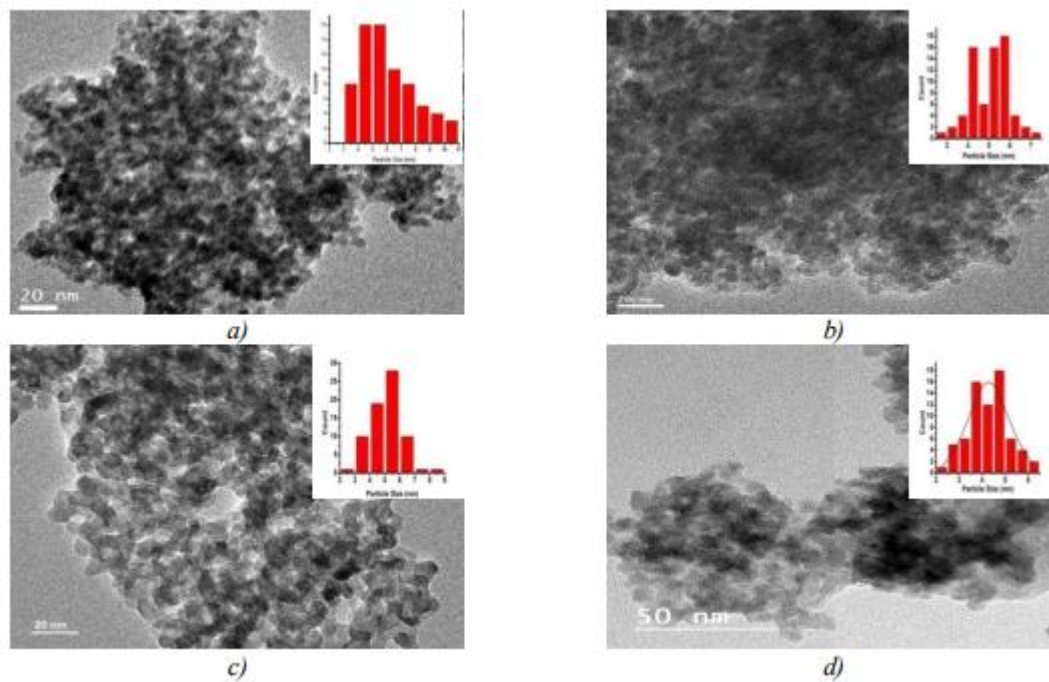
Fig. 4 High resolution TEM micrographs and histogram for a) CdS (b) CdS:Mn (4 wt %), (c) CdS:Mn (8 wt %) and (d) CdS:Mn (10 wt %).

The particle size determined by XRD is less than the one observed in the HRTEM micrograph. One possible explanation is that HRTEM measures all of the sample's structural layers simultaneously, while X-ray diffraction relies on the average sample size found in the XRD pattern, which is smaller. Standard mistakes in the system were not also removed by the XRD approach.
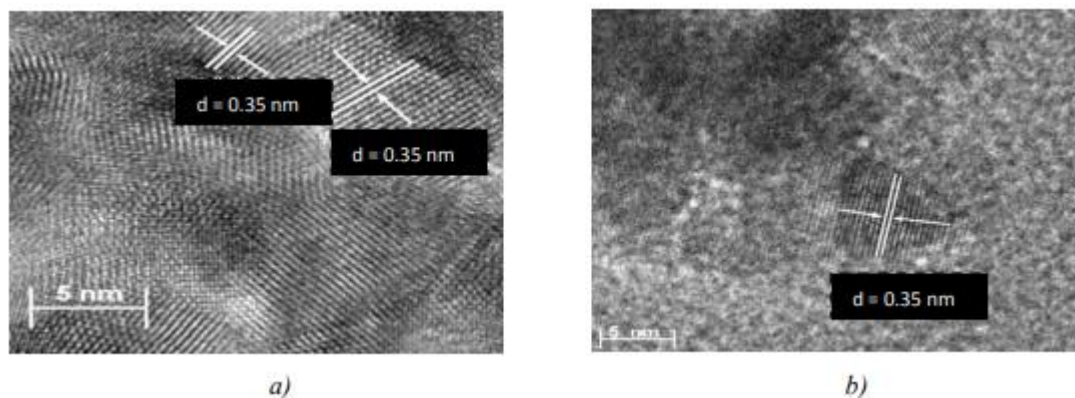
Fig. 5. HRTEM micrographs of crystalline lattice fringes for a) undoped CdS and (b)CdS:Mn (10 wt %)

The crystalline lattice fringes are vividly shown in Figure 5. The HRTEM micrographs revealed an interplanar lattice spacing of approximately 0.35 nm for both undoped and Mn-doped CdS (10 wt %). In agreement with the XRD findings, the measured interplanar lattice spacing value corresponds to the (111) plane of the cubic phase in the produced samples.
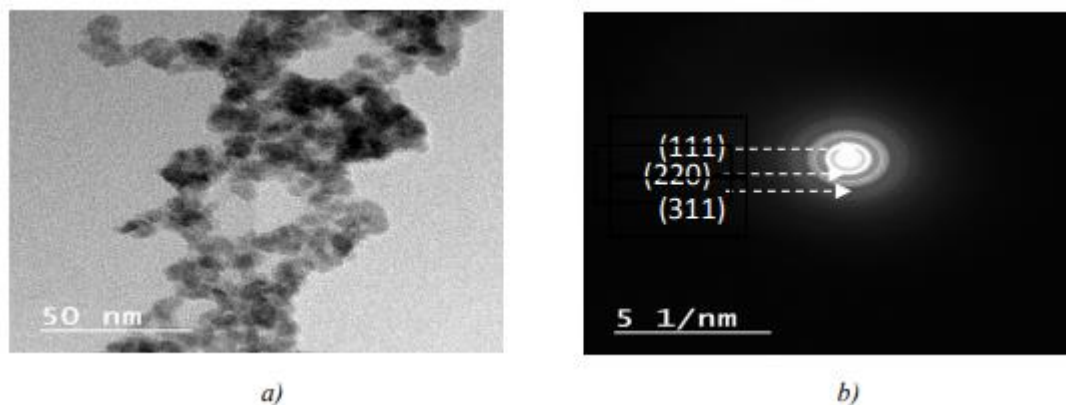
Fig. 6. a) HRTEM image and b) (SAED) pattern of the undoed CdS sample

Figure 6, which shows a HRTEM picture of pure CdS NPs with a selected area electron diffraction (SAED) pattern, shows that the NPs are polycrystalline. As the (111), (220), and (311) planes of the cubic phase, the SAED pattern's rings are indexed accordingly. By applying the following Eq. to all diffraction rings, we have approximated the imaged interplanar lattice spacing (d);

$$d = \lambda L / R \qquad (4)$$

Photoluminescence Studies

The emission of photoluminescence (PL) is a crucial physical property of CdS NPs. Surface state-related PL emission influenced by form, synthesis parameters, size, and energetic location A JASCO-FP-6300 fluorescence spectrometer was used to measure the spectra, with an excitation wavelength of 350 nm.
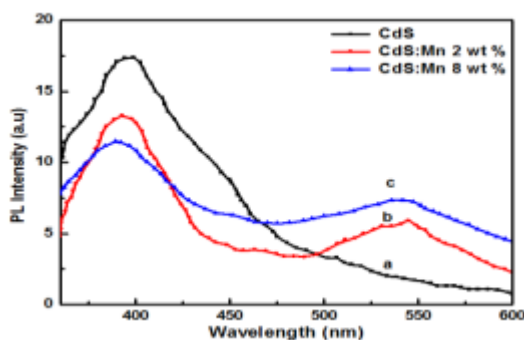
Fig. 9. Photoluminescence spectra for a) CdS, (b) CdS:Mn (2 wt %) and (c) CdS:Mn (8 wt %).

The PL emission spectra of undoped and doped CdS NPs with 2, and 8 weight percent Mn are shown in Figure 9. No emission was observed in the recorded PL spectra of an aqueous surfactant solution devoid of NPs when subjected to the same excitation. The photophysical characteristics of CdS nanoparticles are size and surface passivation dependent, according to this finding. A broadening of the peaks is indicative of nanoparticle production. Excitation of an undoped CdS sample with 350 nm light produces a wide peak with a centre at 410 nm. In the visible spectrum, between 400 and 520 nanometres, CdS phase nanoparticles exhibit their distinctive emission peak. The emission that occurs close to the band gap, or at peaks centred at 410 nm, is caused by electron-hole recombination. A new peak at about 550 nm and a minor blue shift in the typical emission peak of CdS were seen in samples of Mn-doped CdS NPs (2 and 8 weight percent)

when compared to samples of undoped CdS. The peak at 550 nm is caused by the transition of Mn+2 ions inside a nanocrystalline CdS lattice from their 4T1 excited state to their 6A1 ground state. The inclusion of Mn in the CdS lattice was confirmed in the last debate. According to XRD measurements, the particle size reduced as the Mn content increased due to the confinement effect. Even if the emission peak moves to the blue when particle size decreases and surface defects are present, the latter might allow Mn ions to gather positive charges at defect locations. The emission process of CdS:Mn NPs is illustrated in Figure 10, a schematic energy diagram.
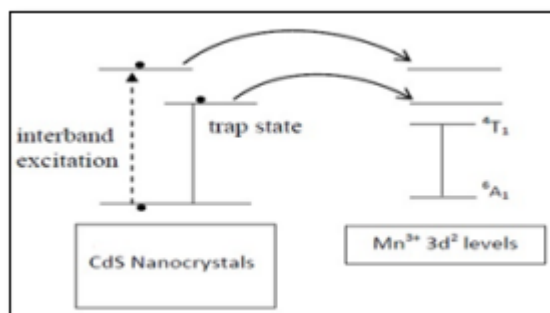
Fig. 10 Schematic diagram of the excitation of Mn+2 in CdS nanocrystals.

Table 4 Differences in emission peak between unadulterated and CdS nanoparticles doped with Mn.

Sample code	Samples	1st emission peak (nm)	2nd emission peak (nm)
S1	Pure CdS	410	----
S2	CdS doped 2% Mn	405	550
S5	CdS doped 8% Mn	400	550

The change in photoluminescence peak with wavelength for S1, S2, and S5 is presented in Table 4. There is a possibility that surface imperfections are responsible for this fluctuation in peak energy.

Conclusion

Doping is an essential component in the process of altering the optical and structural properties of semiconductor nanoparticles. This enables the nanoparticles to be tuned for use in optoelectronics, photovoltaics, sensors, and photocatalysis with specific applications. This work indicates that the inclusion of dopants causes considerable changes in crystallinity, lattice parameters, and defect states. These changes have a direct impact on the structure of the electronic band as well as the dynamics of charge carriers. Doping is shown to impart lattice strain and modify particle shape, as demonstrated by structural analysis. Optical investigations, on the other hand, indicate bandgap tuning, increased or quenched photoluminescence, and defect-mediated emission properties. The findings draw attention to the fact that controlled doping has the potential to enhance light absorption, charge carrier separation, and quantum efficiency. As a result, it is a strong method for boosting the functioning of semiconductor materials. However, optimising the concentration of the dopant and the circumstances of the synthesis are still

extremely important in order to achieve the necessary characteristics without sacrificing the stability of the material. The exploration of novel dopants, the development of more advanced synthesis procedures, and the incorporation of doped semiconductor nanoparticles into functional devices should be the primary focus of potential future study. In addition, a more in-depth comprehension of the interactions between dopants and defects at the nanoscale has the potential to additionally enhance performance and expand the range of applications in the field of next-generation nanotechnology.

References

[1] R. N. Bhargava, D. Gallagher, T. Welker, J. Lumin. 275, 60 (1994).

[2] Ying Wang, N. Herron, J. Phys. Chem. 95, 525 (1991).

[3] M. Ramrakhiani Piyush Vishwakarma, P. Singh, D.P. Bisen,The Open Nanoscience Journal 5, 34 (2011).

[4] J. K. Furdyna, J. Appl. Phys. 64, 29 (1988).

[5] S. Rite John, S. Florence, Chalcogenide Lett. 6, 535 (2009).

[6] S. Rahman, K. Nadeem, M. A. Rehman, M. Mumtaz, S. Naeem, I. L. Papst, Ceram. Int. 39, 5235 (2013).

[7] S. W. Yao, Y. X. Han, W. X. Liu, W. G. Zhang, H. Z. Wang, Mater.Chem. Phys. 101, 247 (2007).

[8] M. Ethayaraja, C. Ravikumar, D. Muthukumaran, K. Dutta, R. Bandyopadhyaya, J. Phys. Chem. 111, 3246 (2007).

[9] L. M. Qi, H. Colfen, M. Antonietti, Nano Lett. 1, 61 (2001).

[10] L E Brus J. Chem. Phys. 79, 5566 (1983).

[11] W. Chen, Z.G. Wang, Z.J. Lin, L.Y. Lin, J. Appl. Phys. 82, 3111 (1997).

[12] T. Arai, T. Yoshida, T. Ogawa, J. Appl. Phys. 62, 396 (1987).

[13] M. Agata, H. Kurase, S. Hayashi, K. Yamamoto, Solid State Commun. 76, 1061 (1990).

[14] P. H. Borse, N. Deshmukh, R. F. Shinde, S. K. Date, S.K. Kulkarni, J. Mater. Sci. 34, 6087 (1999).

[15] A. Lusson, J. Wagner, M. Ramsteiner Appl. Phys. Lett. 54, 1787 (1989).

[16] A. Lewicki, A.I. Schindler, P.M. Shand, B.C. Crooker, J.K. Furdyna, Phys,Rev. B 44, 6137 (1991).

[17] A. Gadala, M. S. Abd El-Sadek, R. Hamood, Chalcogenide Letters 14, 239 (2017).

[18] Ruby Chauhan, Ashavani Kumar, Ram Pal Chaudhary, Res Chem Intermed 39, 645 (2013).

[19] Jamil K. Salem, Talaat M. Hammad, S. Kuhn, Mohammed Abu Draaz, Naser K. Hejazy, R. Hempelmann, J Mater Sci: Mater Electron 25, 2177 (2014).

[20] S Muruganandam, G Anbalagan, G Murugadoss, Indian J Phys 89, 835 (2015).

[21] Nikita H. Patel, M.P. Deshpande, Sandip V. Bhatt, Kamakshi R. Patel, S. H. Chaki, Adv. Mat. Lett. 5, 671 (2014).

[22] M. Thambidurai, N. Muthukumarasamy, S. Agilan, N. Sabari Arul, N. Murugan, R. Balasundaraprabhu, J Mater Sci 46, 3200 (2011).

[23] A. K. Kole, P. Kumbhakar, Appl Nanosci 2, 15 (2012).

[24] Jianing Zhao, Xiaoli Li, Zhiguo Li, Journal of Nanomaterials 2015, (2015).

[25] M. KARMAKAR, O. MONDAL, B. ROY, P. K. PAUL, M. PAL, NANO: Brief Reports and Reviews 8, 1350058 (2013).

[26] S.Aksu, E.Bacaksiz, M.Parlak, S.Yılmaz, I.Polat, M.Altunbaş, M.Türksoy, R.Topkaya, K.Özdoğane, Materials Chemistry and Physics 130, 340 (2011).

[27] Hamed Rahimi, Ali Ghasemi, Reza Mozaffarinia, Majid Tavoosi, J Supercond Nov Magn 29, 2041 (2016).